Oxygen Vacancy Controlled Hyperbolic Metamaterial based on Indium Tin Oxide (ITO) Nanotubes with Switchable Optical Properties

Thomas Herzog,[a,b]‡ Atefeh Habibpourmoghadam,[b,c]‡, Sonja Locmelis,[a] Antonio Calà Lesina,[b,c],* Sebastian Polarz[a],**

a) Institute for Inorganic Chemistry, Leibniz University Hannover, Hannover, 30167, Germany

b) Cluster of Excellence PhoenixD, Leibniz University Hannover, Hannover, 30167, Germany

c) Hannover Centre for Optical Technologies, Leibniz University Hannover, Hannover, 30167, Germany

KEYWORDS: metamaterials, nanotubes, optical anisotropy, infrared plasmonics, transparent conducting oxides

ABSTRACT: Nanostructured metamaterials can offer optical properties beyond what is achievable in conventional media, such as negative refraction or sub-wavelength imaging. Due to their structural anisotropy, the class of high aspect ratio metamaterials is of interest for the possibility of achieving hyperbolic behavior, i.e., materials with both metallic and dielectric optical response based on the excitation direction. Although widely investigated numerically, the

fabrication of tailor-made metamaterials is very complex or often beyond range using current technology. For wire metamaterials composed of aligned metallic nanowires in a dielectric matrix, since the free carrier concentration in metals is fixed, light-matter interaction cannot be adjusted/ changed anymore after fabrication. Here, we introduce high aspect ratio metamaterial based on plasmonic ITO nanotubes with controllable hyperbolic response. The synthesis is achieved by a scalable template-based liquid-phase technique. Our tuning mechanism is based on controlling the carrier density in ITO via oxygen vacancy concentration. The process is reversible, the photonic features are activated by creating oxygen vacancies and can be switched off by filling them up again. Further, it is shown that the carrier concentration can also be controlled via a static electric field. Optical simulations support the experimental findings and highlight the parameters that determine the optical response of the metamaterial.

Introduction

In the past years, metamaterials gained strong attention and paved the way for new and previously unachievable optical effects. Metamaterials are formed by nanostructures of subwavelength size arranged in space with inter-distance smaller than the light wavelength, leading to effective optical properties not available in conventional materials. This enabled the development of new optical components such as metalenses, photonic circuits, and materials with negative refraction.[1–4] Near-field interactions of the incidence light with highly ordered nanostructures result in a collective optical response of the metamaterial that can be tuned by the shape, arrangement, and composition of the individual meta-atoms.[5–7] This collective response is based on the excitation of coupled and localized surface plasmons or Mie resonances inside the metamaterial by electromagnetic waves. The most investigated bulk metamaterials are composite

materials of classical plasmonic metals, like gold or silver, embedded in a dielectric matrix, which can be air in the easiest configuration or other dielectrics, such as alumina or titania.

A special class of metamaterials is metasurfaces, which are two-dimensional arrays of plasmonic or dielectric nanostructures. In contrast to plasmonic metasurfaces, in three-dimensional metamaterials, the plasmonic material exhibits a significant extension in the third spatial direction, which can be chosen to be even longer than the wavelength of the incidence radiation. In such materials, which can be stacks of alternating metallic and dielectric layers or aligned nanowires in a dielectric matrix, an anisotropic optical behavior can be introduced, leading to a material that acts in one direction as a dielectric and in the perpendicular direction as a metal. Such highly anisotropic materials can exhibit a hyperbolic dispersion with one spatial component of their permittivity (ε) opposite in sign to the other two spatial components. Hyperbolic metamaterials (HMM) find applications in sub-wavelength light manipulation and imaging[2,8], sensing[9], and engineering of photonic density of states.[10]

The first experimental example of a hyperbolic metamaterial at visible frequencies was introduced by Yao *et al.* in 2008.[1] In their work, they described the negative refraction of polarized light within a bulk nanowire metamaterial for all incidence angles. The metamaterial was made of aligned silver nanowires with diameter and interspacing much smaller than the wavelength of optical frequencies. It was prepared by electrodeposition of silver nanowires in a porous alumina template (AAO), an easy and low-cost approach for generating metal nanowires that was introduced by Martin *et al.*[11] Thereby, the porous alumina template acts as the dielectric matrix and the silver nanowires as plasmonic antennas, creating the anisotropic optical structure. Depending on the polarization of the incident light, the beam is refracted positively (TE polarization) or negatively (TM polarization). The described findings drew attention for nanowire

3

metamaterials prepared using AAO membranes and their optical properties. Various nanowire dimensions, shapes, arrangements, and materials were investigated for customized applications.[12,13] The vast majority focused on metallic nanowires (mainly Au and Ag) embedded in AAO since their region of operation is in the UV and visible range of the electromagnetic spectrum.[14] Several factors are limiting the applications of metal-based HMMs. For plasmonic and hyperbolic materials incorporating metallic constituents, high optical losses and energy dissipation in the visible and ultraviolet (UV) spectral range have been observed since their interband transitions are also located near these frequency ranges for the metallic components.[15,16]

To overcome these limitations, the search for alternative plasmonic materials delivered new perspectives for hyperbolic and plasmonic metamaterials. Establishing transparent conducting oxides (TCOs) as IR plasmonic materials extended the range of the metal-like constituents in the metamaterial structures.[17–19] Besides the reduced optical losses in the ultraviolet (UV) and visible (Vis) regions of the electromagnetic spectrum, TCOs offer further advantages compared to metals. The free electron concentration in the metallic part of the nanostructures determines the frequency range of the (coupled) plasmonic resonances.[14] For TCO materials, the free carrier concentration can be tailored for the desired operation window – e.g. to technically relevant near-IR wavelengths, including the conventional telecom wavelength (1550 nm).[20] Moreover, most TCOs allow for fine-tuning of the resonance position either by adjusting their doping level or by post-processing. For the most prominent TCO material, Indium Tin Oxide (ITO), the spectral position of the resonance is shown to be dependent on the tin content[5] and additionally on the amount of oxygen, which is present during the deposition[21–24] or an additional post-annealing step.[25,26]

For TCOs and especially ITO, the free carrier concentration can be dynamically and reversibly tuned by external stimuli after their synthesis, enabling a refractive index change of the material.[27]

This effect can be utilized for dynamic reflection, phase and polarization modulation[20,28,29], beam steering applications[30,31], tunable absorbers[32], optical switches[33], and wavefront control.[34] The change in the refractive index thereby is based on the excitation or accumulation of free charge carriers in (a part of) the active ITO material thus altering the refractive index and plasma frequency of this layer.[35] The trigger for the switching can thereby be either electrical or optical. All-optical modulation is based on the intraband pumping of the TCO material, resulting in a strong change of electron distribution and a significant plasma frequency modulation.[36–38] Electro-optical modulation is based on the accumulation (or depletion) of charge carriers in the active material at an interface with a dielectric material.[31,35] Therefore, a layered nanocapacitor structure is required. When a voltage is applied to the capacitor, a very thin carrier accumulation (or depletion) at the TCO/dielectric interface is formed, rendering the TCO material more metallic.[35]

The most common technique for the deposition of ITO with optical quality are physical vapor deposition (PVD) processes.[33,39,40] However, for creating 3D bulk metamaterials, for example, PVD is not applicable by a template-based approach since the penetration depth of the deposited TCO into the nanoscale templates is limited. Liquid phase deposition (LPD) offers an alternative to preparing 3D bulk metamaterials in a template-based approach. The precursor for the TCO material penetrates the template and is converted into metal oxide at the specified location. LPD offers the opportunity to use various templates without needing a catalyst or a pre-patterning step. As described above, AAO templates are a versatile platform for fabricating bulk metamaterials as they not only direct the growth of the metal-like material but also act as the dielectric matrix, e.g., in HMMs.[13] LPD of a TCO in AAO can be a cost-effective and scalable method for producing large area high aspect ratio wire metamaterials.

In this work, we describe a new liquid-phase deposition approach for ITO nanomaterials with controlled optical properties. The process enables the deposition of ITO with high carrier concentrations required for near-infrared (NIR) active metamaterials. A post-annealing step allows for the precise tuning of the oxygen vacancy concentration in the material and control of the operating window of the active ITO material. Nanotubular ITO structures in a dielectric AAO template are formed utilizing the LPD approach with precise morphology control, showing distinct plasmon resonances in the NIR. The ITO nanowires embedded in the dielectric alumina matrix exhibit anisotropy in the permittivity parallel and perpendicular to the nanotube axis, which can be tailored by the post-annealing treatment. Full wave simulations of the new metamaterial confirm the optical anisotropy and highlight the most relevant parameters that determine the optical response of the material, including a hyperbolic behavior in the NIR region.

Results

The LPD of the ITO thin film and nanotubes is carried out in a three-step process. For thin films and nanotubes, a silicon wafer coated with a thin titanium and wolfram adhesion layer is used **(Scheme 1)**. On top of the adhesion layers, a thick aluminum layer (1000 – 5000 nm) is introduced. The top of the aluminum layer is either converted into a plane aluminum oxide (AO) or a porous anodic aluminum oxide (AAO) layer by an electrochemical oxidation procedure for preparing thin films or nanotubes, respectively.[41] The substrate is immersed in an ITO precursor solution containing indium and tin salts in a molar ratio of 9:1 In : Sn to achieve a doping level of 10% for the resulting materials (see Methods section). For this doping level, the highest free charge carrier concentrations and plasmonic resonances in the IR range can be achieved.[5,42] After immersion of the substrates/templates, the excess precursor solution is removed by spin coating, and the

precursor is converted to ITO by thermal treatment at 300°C in air. Finally, a high-temperature post-annealing is conducted to increase the crystallinity of the ITO and to alter the charge carrier concentration in the material.
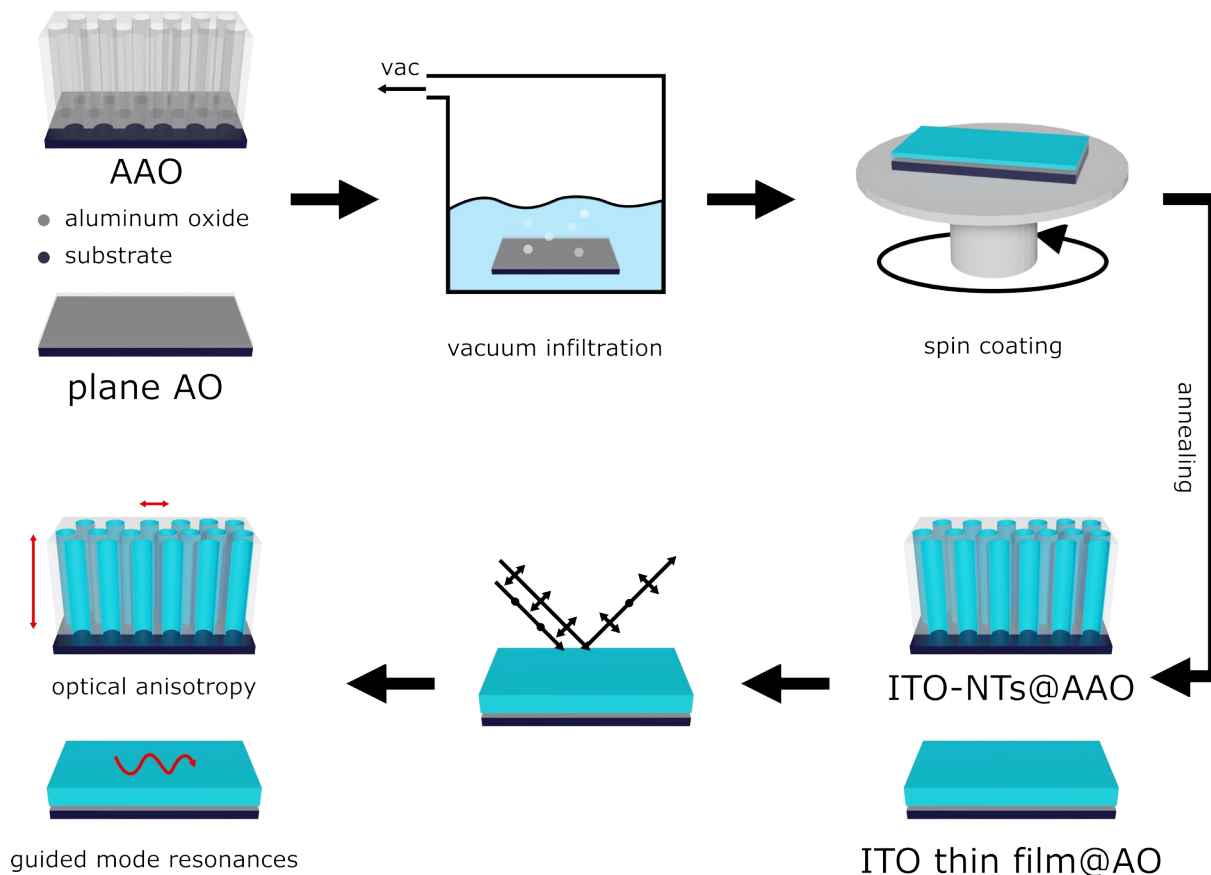

Scheme 1. Fabrication of optical ITO coatings and nanowire arrays.

Influence of Processing Parameters on Permittivity of ITO. The plane materials will be discussed first. The structure of the ITO thin films after the post-annealing is shown in **Figure 1**. On top of the Al back-side mirror and the thin film of AO (30 nm), a uniform ITO layer with a thickness of 100 nm is formed after 4 deposition cycles. The grain boundary structure of the ITO film can be observed in the SEM image. Before the post-annealing step, the ITO film exhibits a low crystallinity as evidenced by x-ray diffraction. After annealing at 450°C, the crystallinity of the ITO layer strongly increases (Figure S1). A good crystallinity is crucial for optical and

electrical applications to achieve a high carrier concentration and to reduce grain boundary scattering and defect states. The charge carrier density, which determines the optical and electrical behavior of ITO, is mainly dependent on two doping mechanisms (Figure 1a) – the Sn^{4+} and the oxygen vacancy doping. Replacing an In^{3+} ion with a tetravalent Sn^{4+} n-type doping of the ITO is achieved, generating free electrons in the conduction band. The same applies to oxygen vacancies; two electrons are donated to the conduction band for each missing oxygen atom in the structure. As described above, a Sn-doping level of 10% is intended for the ITO films since this doping level is expected to lead to the highest charge carrier concentration. The doping level of the ITO film was determined by x-ray photoelectron spectroscopy (XPS, Figure 1c,d) and energy-dispersive x-ray spectroscopy (EDX) to be ~ 10%. This doping level is chosen for the whole work.

The oxygen vacancy doping can be tailored by the post-annealing treatment. Therefore, the samples are annealed at 450°C for 3 h in different atmospheres (O_2, Ar, vacuum /10^{-1}, 10^{-2}, 10^{-3} mbar and H_2/Ar). The customized oxygen content or the reducing gas (H_2/Ar) in the annealing atmosphere has a strong influence on the composition (Figure 1) and optical properties of the ITO film. The film without post-annealing treatment (as-prepared) and the films annealed in O_2 and Ar atmosphere show a high diffusive reflectance (>80%) in the visible range, indicating a low absorbance by the ITO film (Figure S2). A clear trend to a reduced reflectance (higher absorption of ITO) with higher vacuum conditions is noticeable for the vacuum-annealed films. The reasons for the higher absorption of the vacuum-annealed films are twofold. Due to the more metallic behavior of the samples, lossy or guided mode resonances can be introduced in the ITO film (Figure S3).
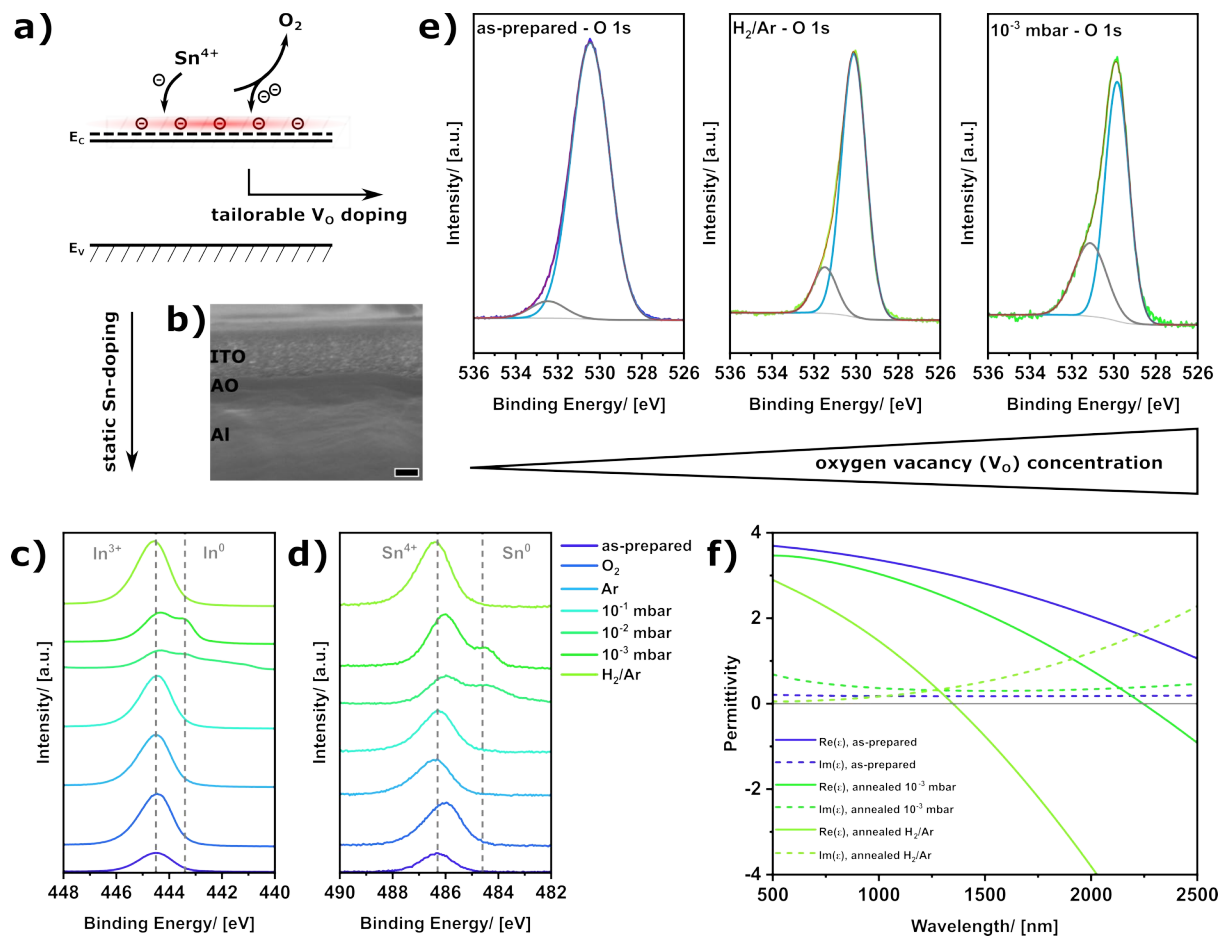
Figure 1. Doping mechanisms in ITO thin films. Scheme of the band structure of ITO with an indication of the two doping mechanisms to increase the free charge carrier amount (a) – static doping by introducing Sn^{4+} ions and tailorable doping by removing oxygen, resulting in oxygen vacancy (V_O) doping. SEM image of the ITO film deposited on an aluminum substrate with a thin aluminum oxide (AO) layer (b, scale bar 50 nm). Core level XPS spectra for In (c) and Sn (d) after annealing in different atmospheres. O 1s core level spectra for three samples (e) - without post-annealing (left, as-prepared), with post-annealing in H_2/Ar atmosphere (middle), and with post-annealing under reduced pressure (right, 10^{-3} bar). For each spectrum, the deconvolution of the O 1s peak in the contribution of lattice oxygen (blue peak) and non-lattice oxygen (grey peak) is shown, indicating the increasing amount of oxygen vacancies with the different annealing conditions. The real and imaginary part of the permittivity of the three samples (f).

Additionally, metallic impurities can be generated in the films due to the reduction of In^{3+}- or Sn^{4+}-ions when a high amount of oxygen vacancies is generated, tailoring the doping efficiency of the Sn-doping. This phenomenon appears in the XPS core level spectra of In and Sn (Figure 1c,d). Besides the peaks for In^{3+} and Sn^{4+} in the oxide at binding energies of 444.5 eV and 486.3 eV, respectively, peaks for metallic In^0 and Sn^0 appear for the high vacuum (10^{-2} and 10^{-3} bar) annealed samples. Only a Gaussian peak for In^{3+} and Sn^{4+} is observed for all other samples, indicating no interfering metallic impurities in the films. Although there are no metallic impurities in the films annealed under a pressure of 10^{-1} mbar and under reducing gas (H_2/Ar, 5%/95%) there is an increased absorption of the ITO film, which can probably be attributed to resonance modes of the films based on the increased carrier concentration.[25] The effect of the post-annealing on the oxygen vacancy concentration is visible in the XPS O 1s core level spectra (Figure 1e) since the binding energy for the oxygen vacancies (non-lattice oxygen) is slightly higher than for the lattice-bound oxygen. By deconvolution of the O 1s peak for the as-prepared, the H_2/Ar annealed, and the high vacuum annealed (10^{-3} mbar) sample, the amount of oxygen vacancies (V_O) in comparison to the lattice oxygen in the films can be determined. For the as-prepared sample, a very low amount of oxygen vacancies of around 3.6% is found, which is consistent with the high reflectivity of the sample. The oxygen vacancy concentration increases for the H_2/Ar annealed sample to 13.1% and 21.8% for the high vacuum annealed sample. This high vacancy content in the vacuum-annealed samples is probably the reason for generating metallic impurities.

The doping level and the composition of the film are related to its optical properties and plasmonic behavior via the refractive index and the dielectric permittivity. The dispersion of the permittivity (Figure 1f) and refractive index of the ITO films is determined by spectral ellipsometry (Figure S4). As shown in Figure 1f, the dispersion of the permittivity is strongly

tailored by the post-annealing process. The as-prepared ITO film shows dielectric behavior over the whole investigated range, whereas the vacuum annealed and the H_2/Ar annealed samples show a transition from positive to negative permittivity in the IR range at a wavelength of 2253 nm or 1349 nm, respectively. Remarkably, the transition for the vacuum annealed sample is at a higher wavelength than for the H_2/Ar annealed sample, although the V_O doping level is higher, indicating that the free carrier concentration for this ITO film is lower. An explanation for the behavior can be the inhomogeneity and the high defect density of the vacuum-annealed films, which is also indicated by the metallic impurities in the material. Most interesting for NIR plasmonic applications is the H_2/Ar annealed sample since its epsilon near zero (ENZ) range $(1 > e_{Re} > -1)$ spans from about 1120 nm to 1547 nm with a cross-over wavelength of real and imaginary part of 1278 nm and therefore acts metallic at the relevant telecom wavelength (1550 nm). Additionally, a near-zero-index (NZI)[43–45] condition with $\lambda_{NZI} = 1336$ nm and a bandwidth of 388 nm is observed for the thin films (Figure S4). From the Drude model, a plasma frequency of 2.54×10^{15} rad/s is extracted from the ellipsometry data, indicating a high free carrier concentration of 8.09×10^{20} cm^{-3} that supports plasmon resonances in the NIR. In summary, the results for the ITO thin film show that with the liquid phase deposition process and the post-annealing step, ITO coatings with a tailorable carrier concentration can be prepared, and ENZ and NIZ conditions in the NIR can be reached in the ITO coating.

Fabrication of ITO Nanotube Metamaterial. To exploit the full potential of the LPD nanostructures, optical metamaterials are prepared by the new LPD process. Nanotube-arrays are prepared by a template-based approach, utilizing porous anodic aluminum oxide as a hard template (Scheme 1). The template is vacuum infiltrated with the liquid ITO precursor, then the excess precursor is removed by spin coating, and in the last step, the precursor is dried and converted to

ITO in an oven step. This process is repeated until the desired thickness of the nanotubes is reached. The spin coating step is required to achieve uniform nanotubes; without this step, an ITO layer is generated on top of the template, interconnecting the nanotubes, which would have a great impact on their optical properties (Figure S5). The deposition kinetics is monitored by monitoring the In/Al ratio after representative deposition cycle by EDX **(Figure 2a)**.
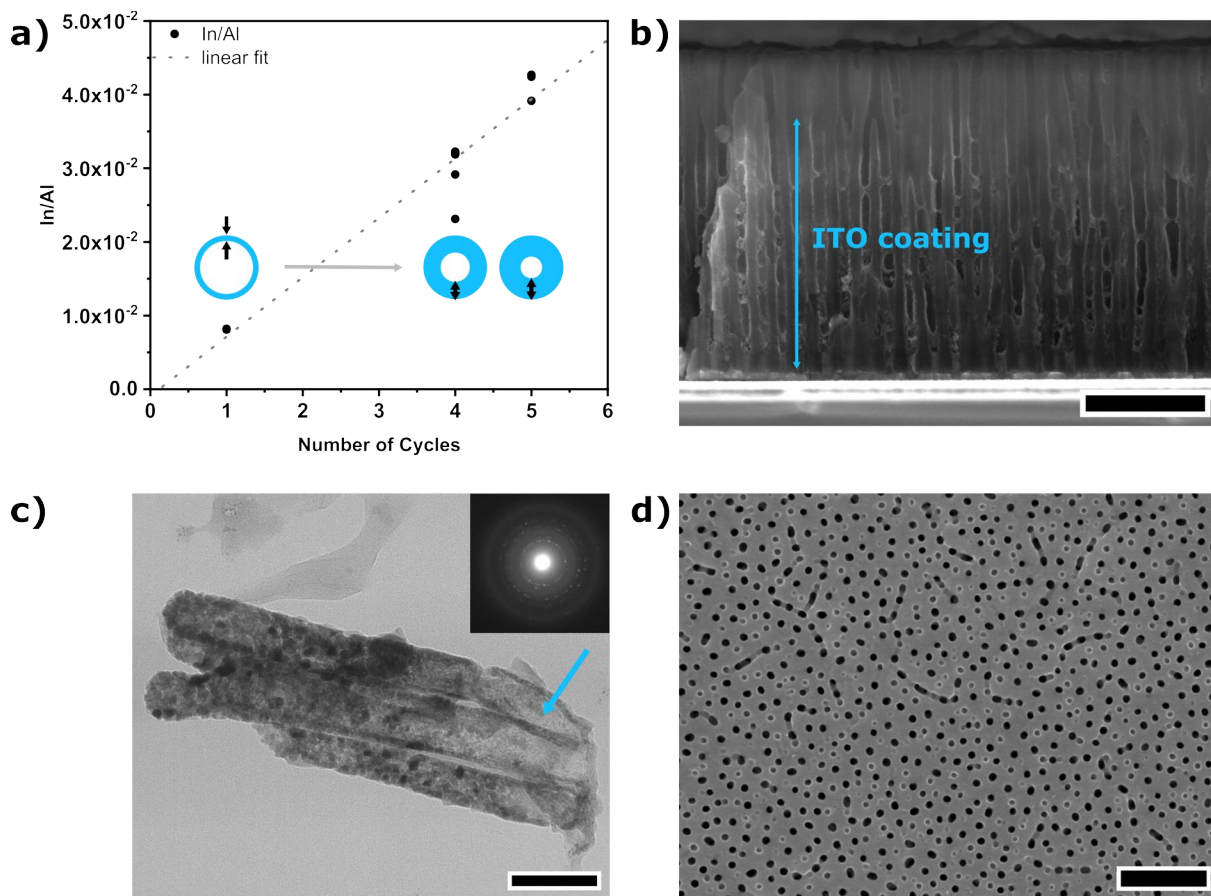
Figure 2. Preparation of ITO nanotubes. Evolution of the In to Al ratio with deposition cycle, indicating the linear increase of In (ITO tube wall thickness) with deposition cycle (a). Side-view SEM image of the ITO-coated AAO template on a tungsten-coated Silicon wafer (b, scale bar 500 nm). TEM image of the ITO nanotubes freed from the AAO membrane (c, scale bar 100 nm). Inset: SEAD pattern of the nanotubes, indicating the polycrystalline nature. Top-view image of the coated AAO membrane (d, scale bar 500 nm).

Since the Al signal originates from the AAO template, it should be constant, and in relation, the In-signal should increase due to the ITO deposition. A linear dependency of the In/Al ratio with deposition cycle is observed, indicating that the growth of the ITO thickness is constant for consecutive cycles, which enables control of the nanotube wall thickness. The wall thickness of hollow structures is an important factor in tuning the plasmon resonances in such materials and is theoretically investigated in the next section.[46] For this work, the number of deposition cycles is chosen to be five, which results in wall thicknesses of about 15 – 20 nm (Figure S6). In the cross-section image of the nanotubes in the AAO template, the filling of the pores with ITO is visible by the slightly brighter contrast of the ITO in comparison to the alumina template (Figure 2b). Before the post-annealing step, the nanotubes are amorphous (Figure S6) and crystallize during the annealing to a polycrystalline structure (Figure 2c). Thereby, larger grains are formed, and the surface gets rougher. The TEM image also indicates that the wall thickness gets thinner at the top of the nanowires (blue arrow) and that the thickness there is insufficient to achieve good crystallinity.[47,48] In the top-view image of the template after the LPD of ITO nanotubes, the absence of an ITO overlayer is visible, all pores are still opened (pore diameter ~ 60 nm), and the structure is intact after the annealing step (Figure 2d). As is evident, all nanopores and, therefore, also the nanotubes are arranged in parallel to each other, but there is no distinct arrangement in the lateral direction.

After the post-annealing step, the nanotubes may be coated with a thin TiO_2 layer to suppress re-oxidation (filling of the oxygen vacancies by ambient oxygen) and degradation of the plasmonic ITO material (Figure S7). To introduce a significant resonance of the ITO nanotubes in the IR range, at least four deposition cycles of ITO are required (Figure S10). For a lower amount of deposition cycles, only a negligible absorption is observed. The absence of the resonance can be

explained by two effects. First, the absorption cross-section for nanotubes with thin (<5 nm) tube walls is vanishingly small. Second, the reduced tube wall thickness leads to poorer crystallinity and reduced charge carrier density and mobility in the ITO material.[47] With increasing deposition cycles the position of the plasmon resonance blue-shifts, which can be assigned to an increased ITO thickness of the tubes and utilized for tuning the metamaterial response (see next section).

Theoretical Description of ITO Nanotube Metamaterial by Effective Medium Theory. Since the nanotube diameter (~60 nm), wall thickness (5-20 nm), and spacing (~100 nm) is small compared to the wavelength of the probe light; it is expected that the material behaves as an effective medium in the visible to NIR wavelength range (500 – 2500 nm). The highly anisotropic structure of the metamaterial is known to introduce an anisotropy in the optical properties expressing itself in the permittivity and refractive index of the material. For wire metamaterial the anisotropy of the permittivity can be predicted by effective medium theory based on the permittivity dispersion of the constituent materials.[49] As is evident from the schematic image of the ITO nanotube array in the dielectric matrix **(Figure 3a)** for the x- and y-direction, a difference in the permittivity compared to the z-direction is expected, since the free electron motion is hindered in the x- and y-direction, whereas it is possible in z-direction inside the nanotubes. For the calculation of the permittivity perpendicular ($\varepsilon_\perp$) and parallel ($\varepsilon_\parallel$) to the nanotubes, a permittivity $\varepsilon_{Al2O3} = 2.4$ and $\varepsilon_{air} = 1$ is assumed for the dielectric material and the hollow material inside the tubes, respectively. The permittivity dispersion of the ITO is taken from Figure 1f for the H$_2$/Ar annealed sample, and a porosity of $p = 0.32$ of the AAO membrane is extracted from SEM images (Figure 2d). The permittivities are determined by the following equations:[49]

$$\varepsilon_\parallel = p(f\varepsilon_{ITO} + (1-f)\varepsilon_{air}) + (1-p)\varepsilon_{Al_2O_3} \tag{1}$$

$$\varepsilon_\perp = \varepsilon_{Al_2O_3} + \frac{p\varepsilon_{Al_2O_3}((f\varepsilon_{ITO}+(1-f)\varepsilon_{air})-\varepsilon_{Al_2O_3})}{\varepsilon_{Al_2O_3}+(1-p)((f\varepsilon_{ITO}+(1-f)\varepsilon_{air})-\varepsilon_{Al_2O_3})q_{eff}} \tag{2}$$

Here ε_{Al2O3} is the permittivity of the Al$_2$O$_3$ matrix, ε_{ITO} is the permittivity of the ITO nanotubes, ε_{air} is the permittivity of air filling the tubes and $f = \pi(r_{ITO}^2 - r_{air}^2)$ is the fill fraction of ITO in the pores. q_{eff} is the depolarization factor perpendicular to the nanotubes and is estimated to be ½.

For the spatial directions perpendicular to the nanotube axis, a pole in the permittivity (ENP) is obtained, which redshifts with decreasing nanotube wall thickness (Figure 3b). The pole in the permittivity can be related to a transversal plasmonic resonance of the nanotubes. In the wavelength range slightly below the pole the material exhibits a negative permittivity, whereas in the other wavelength regions the permittivity is positive and the material is expected to behave like a dielectric. In the direction of the nanowires the material behaves like a metal with a permittivity that decreases with increasing wavelength going from positive to negative sign at the epsilon near zero (ENZ) condition (Figure 3c). The ENZ point also redshifts with decreasing nanotube wall thickness, due to the decreased amount of metal-like material in the nanostructure. For application as an anisotropic metamaterial especially the frequency ranges in which the permittivity is opposite in sign for the parallel and perpendicular direction is highly interesting, since these materials exhibit a hyperbolic dispersion of the wavevector.[14] The areas where hyperbolic dispersion is expected for the ITO nanotube metamaterial with wall thickness of 20 nm is exemplary shown in Figure 3d. In the wavelength range from 1700 nm to the ENP at about 2100 nm e$_\perp$ is negative in sign, whereas e$_{II}$ is positive, indicating type II hyperbolic behavior.[14] For wavelength above the ENZ condition the situation is opposite with $\varepsilon_\parallel < 0$ and $\varepsilon_\perp > 0$ exhibiting type I hyperbolic behavior.
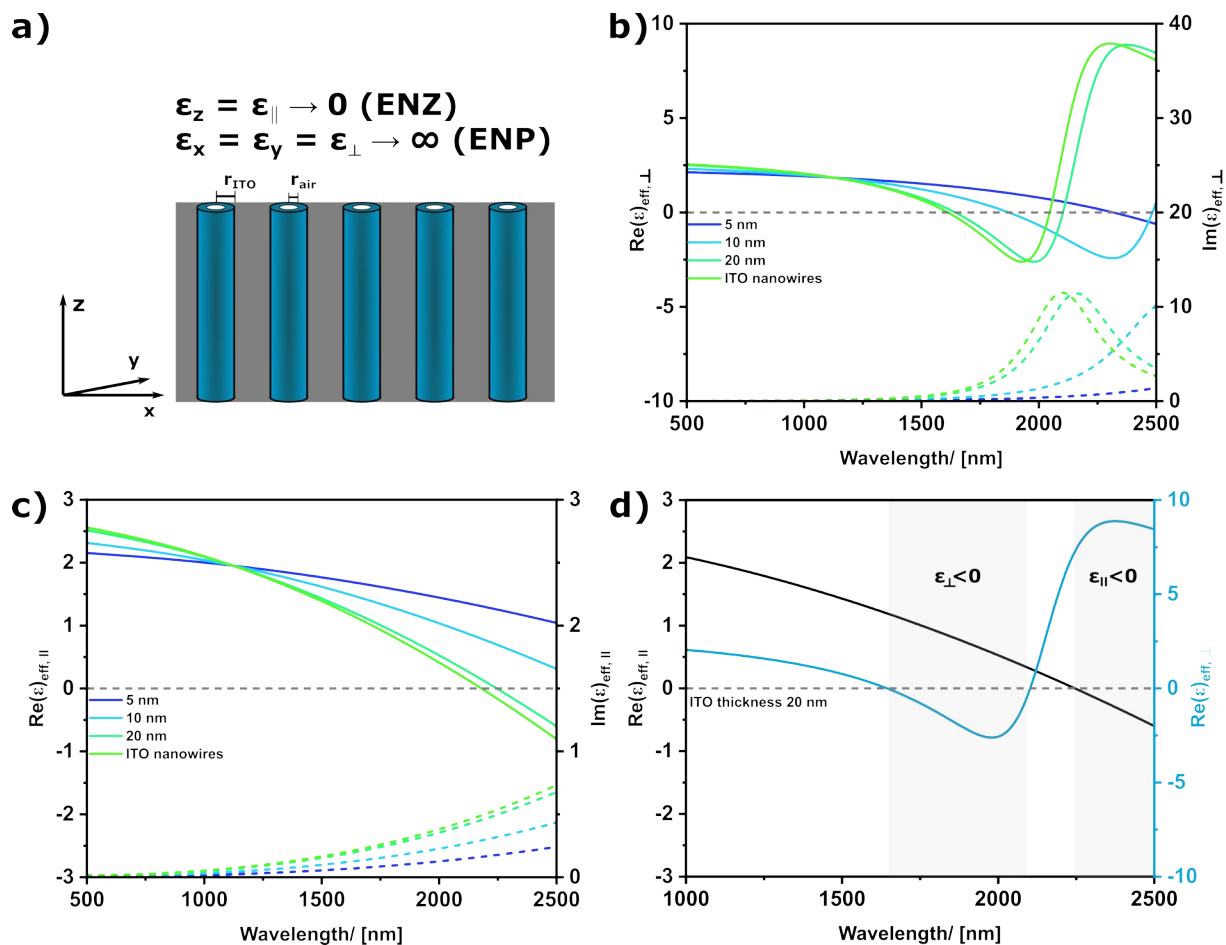
Figure 3. Schematic depiction of nanotube metamaterial cross section indicating the anisotropy in the permittivity perpendicular and parallel to the nanotubes and the orientation of the epsilon near zero (ENZ) and epsilon near pole (ENP) direction (a). Real (straight lines) and imaginary part (dotted lines) of permittivity perpendicular (b) and parallel (c) to the nanotube axis calculated by effective medium theory for different wall thicknesses of ITO tubes (based on the permittivity obtained for the H_2/Ar annealed ITO thin films). Real part of the permittivity for the metamaterial with 20 nm ITO thickness parallel (black) and perpendicular (blue) to the nanowires, indicating the wavelength ranges with opposite sign of the permittivity in the two directions (d).

Influence of Annealing on Experimental Observed Optical Response of the ITO Nanotube Metamaterial. Experimentally, the position of the ENP and, therefore, the upper boundary of the

16

type II hyperbolic range can be determined by extinction and transmission (Figure S11) measurements, as a resonant absorption is expected at the pole, indicated by a maximum of the imaginary part of the permittivity (Figure 3c). For analysis of the hyperbolic properties it is best to study the behavior for s- and p-polarized light separately. S-polarized light has its electric field for all angles of incidence (AOI) in a direction perpendicular to the nanotubes, and due to the sub-wavelength structuration of the material in that direction, it only experiences the effective $\varepsilon_\perp$ **(Figure 4a)**. P-polarized light has a component of its electrical field in the direction of the nanowire long axis for oblique angles and, therefore, is influenced by both $\varepsilon_\perp$ and $\varepsilon_\parallel$ (Figure 4b). The extinction measurements are conducted in diffuse reflectance geometry at an AOI of 45°. The sample is located on a mirror-like substrate during the extinction measurements to back-reflect the transmitted light (Figure 4c). The investigated ITO nanotubes exhibit a high aspect ratio of about 23 (length 1400 nm, diameter 60 nm). Concerning the extinction spectrum for s-polarized light, for wavelengths up to 1500 nm thin film interference fringes are observed, due to the thickness of the AAO membrane with the embedded nanotubes (Figure 4c). Quantitatively, a low absorption is observed over the whole wavelength range for s-polarized light for all samples, which is reasonable due to the small absorption cross-section perpendicular to the nanotubes. As expected from the ellipsometry data no absorption for both polarizations in the NIR range is observed for the sample without the post-annealing step. However, a slight and broad absorption feature is observed in the range from 1600 nm to 2100 nm, with a maximum at about 1860 nm for the H_2 annealed sample, which can be assigned to the ENP. Interestingly also, a small absorption feature is observed for the high vacuum annealed sample, which is at a slightly lower wavelength than for the H_2 annealed sample. As described previously, p-polarized light incidence at oblique angles exhibits a component of the electrical field in the direction of the nanotube long axis (Figure 4c). Due to this

17

component, the absorption cross-section is strongly increased in comparison to the case for the s-polarized light, which can be observed by the increased bandgap absorption at wavelengths below 500 nm for all samples (Figure 4d). As also observed for s-polarized light below 1500 nm the absorption spectra are overlaid with thin film interference fringes. For p-polarized light the absorption peak with a maximum at 1860 nm for the H_2/Ar annealed sample is strongly enhanced, confirming the ENP condition at this wavelength. The high vacuum annealed sample exhibits an even higher absorption maximum with a sharp resonance at 1350 nm and a shoulder at about 1650 nm. So, although the ellipsometry data indicates that there should be no plasmonic resonance of the high vacuum annealed sample in the NIR range it exhibits a strong resonant absorption, which can indicate a higher post annealing efficiency for the nanotubes compared to thin films. As is evidenced from the extinction measurements also the ENP condition for the H_2 annealed material is observed at a lower wavelength than predicted from our EMT calculations. The reason for that is probably also that the annealing step for the nanotubular structures is more effective since the nanotubes are more accessible for the reducing gas atmosphere. Therefore, the plasma frequency is lower than for the thin films, which results in a shift of the ENP conditions to a lower wavelength (see also Figure 5b). An important feature of the materials is that one cannot only activate the photonic features but the plasmon resonances can be turned off by re-oxidation. The latter is shown in Supporting Information Fig. S-12 and the reason for the claim that the presented metamaterial possesses switchable optical properties.
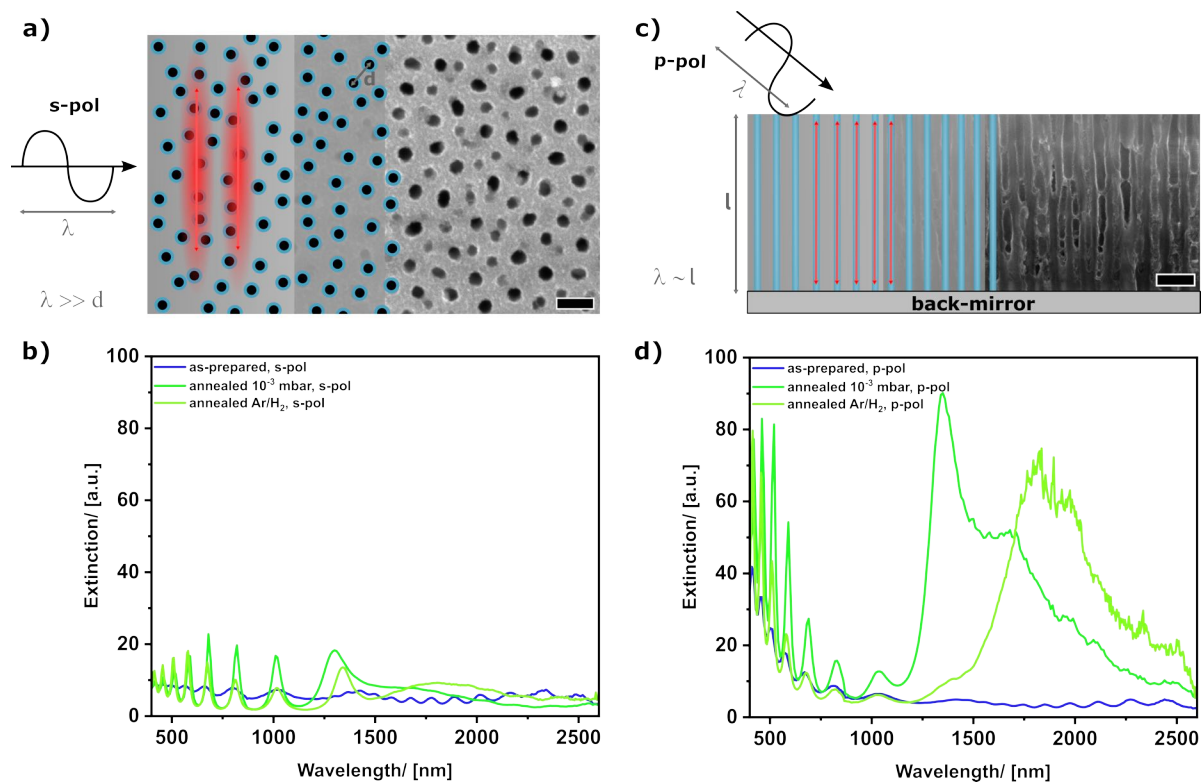
Figure 4. Schematic illustration of the interaction of s- and p-polarized light with the ITO nanotube filled AAO metamaterial (a and c, respectively). Optical absorption spectra extracted from diffuse reflectance measurements for s- and p-polarized light (b and d, respectively).

From the extinction measurements it is clear that for the metamaterial a hyperbolic behavior can be expected in the NIR range and the wavelength range of the hyperbolic behavior can be tailored by the processing conditions and the plasma frequency of the incorporated ITO. As for applications the specular reflectance is more important, it is investigated in the next section and compared to optical simulations to confirm the anisotropy in the permittivity. The difference between extinction measurements and specular reflectance measurements is mainly determined by taking the scattering into account. The extinction spectra can be transformed into reflectance spectra by the Kubelka-Munk transformation. When comparing this calculated reflectance to the actual measured

specular reflectance there are only slight derivations, indicating a negligible influence of the scattering (Figure S12).

Impact of Post-annealing and Nanotube Geometry on Optical Response. The optical response of the metamaterial is simulated based on the geometrical parameters of the metamaterial and the experimental obtained permittivity of the ITO (Figure 1f). Comparison of the experimental results and the full wave simulations highlights the impact of processing parameters on the optical response of the metamaterial. According to the measurement geometry the incident beam is assumed at oblique incident of 45° for both s- and p-polarization. Based on the sample geometry, the AAO membrane coated with ITO is simulated on a tungsten coated silicon substrate. The simulated geometry is schematically shown in Figure 5a. For the main model, the height of the AAO membrane (h) is assumed to be 1400 nm, on a silicon semi-infinite substrate. The nanotubes are arranged in a hexagonal manner and the pore diameter (d) and interpore spacing (s) are extracted from SEM images to be 58 nm and 98 nm, respectively. The tungsten (W) underlayer can have a maximum thickness of 50 nm changing due to the oxidation process. The sum thickness of the tungsten and the tungsten oxide (WO_x) thin layers is equal to 50 nm. From Figure 1f, the plasma frequency of the thin film of ITO is obtained by fitting the experimental data to the Drude model,

$$\varepsilon(\omega) = \varepsilon_\infty - \frac{\omega_p^2}{\omega^2 + i\gamma\omega} \tag{3}$$

where $\varepsilon_\infty = 4.2345$ is the high frequency dielectric constant of the ITO, $\gamma = 1.7588x\ 10^{14}$ rad s^{-1} is the ITO Drude damping factor. From fitting investigations of the permittivity of the H_2/Ar annealed sample, a value of $\omega_p = 2.54x\ 10^{15}$ rad s^{-1} was found (corresponding to the wavelength of $\lambda = 742$ nm). Simulations are performed for ITO coated AAO matrix equipped with a multilayered substrate formed from silicon, tungsten and WO_x. The templates are simulated with

hexagonal periodicity. The plasma frequency and the thickness of ITO are assumed $2.54x\ 10^{15}$ rad s^{-1} and 20 nm, respectively.

Since the thin tungsten layer beneath the AAO template might get oxidized during the nanotube preparation process, a numerical study is conducted to investigate the impact of this oxidation process on the optical response of the material (Figure S13). As already indicated by the theoretical investigations (Section 2.3), the plasma frequency and the ITO thickness are the decisive parameter determining the response of the metamaterial. Tuning of the plasma frequency is also known to open new perspectives towards tunable metamaterials.[30] Figure 5b shows the reflectance spectra obtained for a parametric study on the plasma frequency of the ITO in the hybrid material with a s-polarized (p-polarized, see Figure S15) light beam. For all plasma frequencies a reduced reflectance for higher wavelengths (above ~ 1500 nm) is observed, which is not present for plain AAO templates (Figure S14).

From the simulation data, a blue-shift of the high frequency limit of the plasmonic absorption is observed (black arrow) with increasing plasma frequency of the ITO nanotubes. This blue-shift is also experimentally observed (as indicated in Figure 4), when comparing the reflectance spectra of the H$_2$/Ar annealed sample and the high vacuum annealed sample (Figure 5c). As seen from the theoretical investigations (Figure 3) a variation of the nanotube geometry (wall thickness and length) also has a great impact on the optical response. As observed in the TEM and SEM images (Figure 2) the nanotubes are not perfectly uniform and they exhibit variations in their length and thickness. Therefore, parametric studies concerning the length (Figure S16) and more interestingly concerning the wall thickness (Figure 5d,e) are conducted. As can be seen in Figures 5d and 5e the shape of the absorption band for s- and p-polarized light strongly changes with ITO thickness. Most dominant is the decreasing reflection with increasing wall thickness, which can be attributed

to the higher amount of ITO in the metamaterial, which is in line with the experimental observations (Figure 5c, Figure S10).
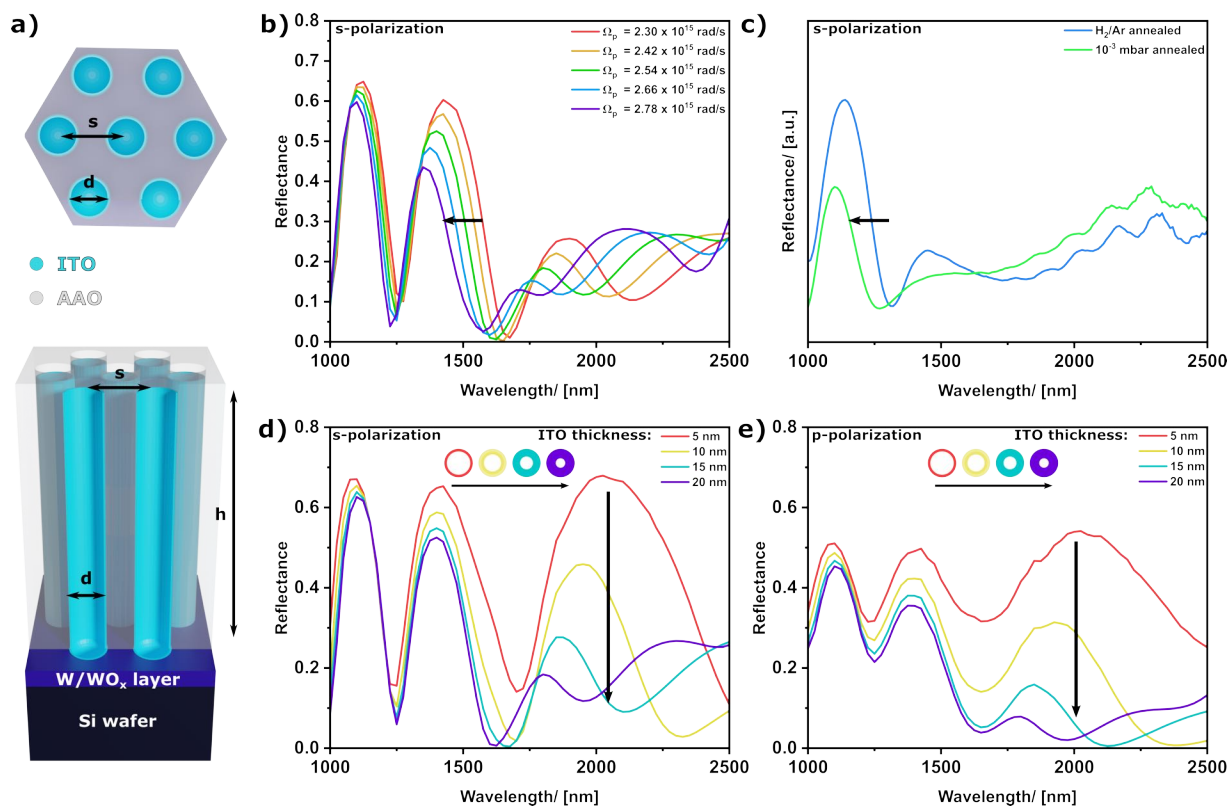
Figure 5. Structural model to determine reflectance spectra by full wave simulations (a). Simulated reflectance spectrum for s-polarized light for different plasma frequencies (b). Experimental determined reflectance spectra for the H_2 (blue) and high vacuum annealed sample for s-polarized light (c). Simulated reflectance spectra for different ITO thicknesses for s- (d) and p-polarized (e) light.

There is additionally a slight blue-shift of the resonant absorption as predicted by effective medium theory (Section 2.3). As seen from **Figure 6**, for both polarizations the reflectance is reduced at the wavelengths in the range of the expected hyperbolic behavior. As expected from the structural anisotropy induced by the ITO nanotubes there is a different response to s- and p-polarized light at a given incident angle.

22
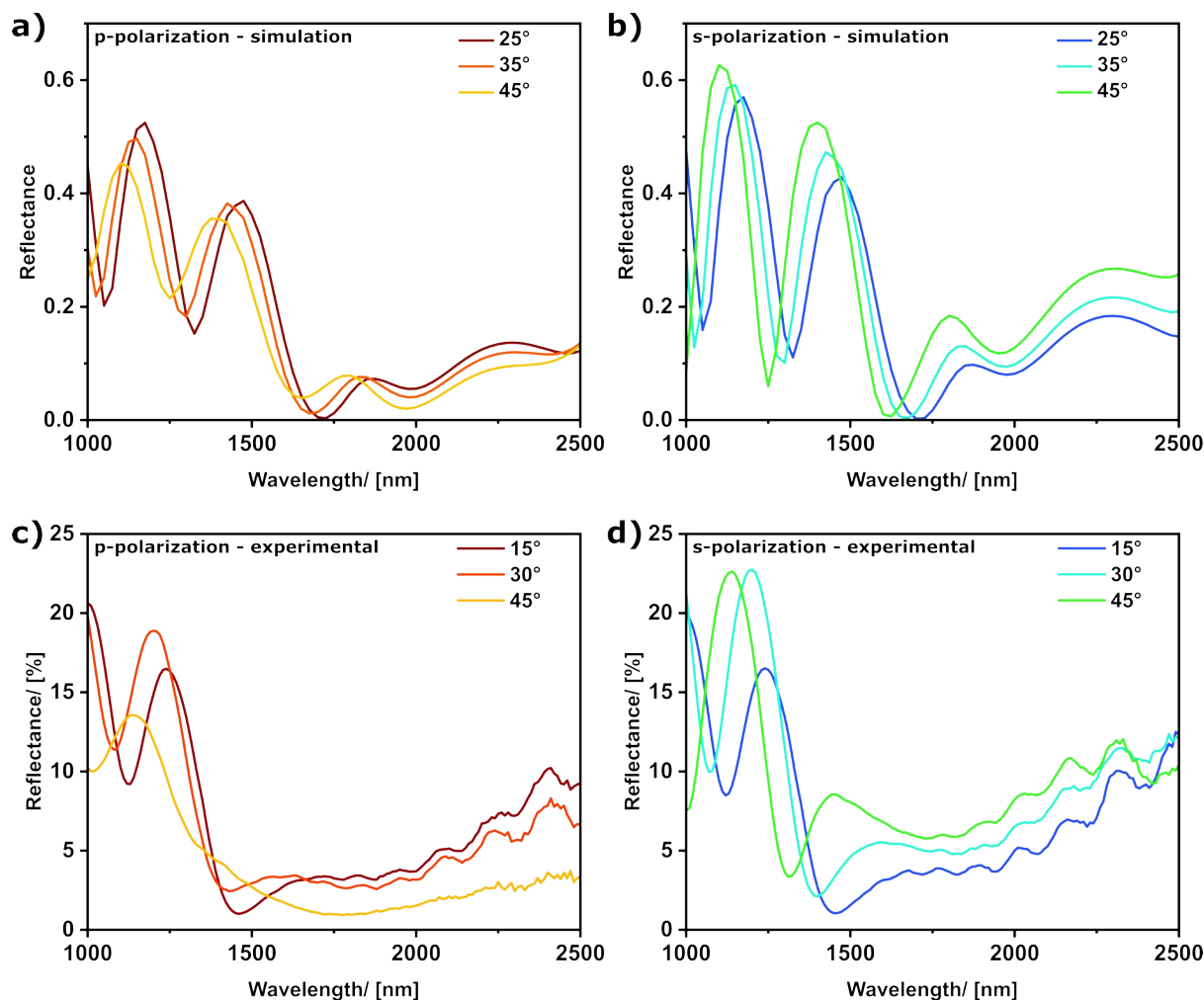
Figure 6. Simulated reflectance of the ITO nanotube arrays in the dielectric matrix for different AOIs for p- (a) and s-polarized (b) light. Experimental observed reflectance spectra for the H_2/Ar annealed sample for p- (c) and s-polarized (d) light incidence at different angels.

Since it is not possible to directly measure hyperbolic behavior the spectral reflectance spectra of the two samples for s- and p-polarized light and various AOI are evaluated (Figure 6, S17 for the high vacuum annealed sample) to confirm the presence of hyperbolic behavior[14], beside the indications from the extinction spectra and EMT. As is expected for all samples, all AOI and both polarizations in the range of the ENP resonance (1500 nm – 2500 nm) the reflection is strongly reduced. Due to the structural and optical anisotropy of the metamaterial the response for different

23

AOIs is expected to differ, since the interaction strength with the perpendicular and parallel permittivity is altered by the angle of incidence. For p-polarized light the reflectance significantly decreases with increasing AOI and the absorption band seems to broaden with increasing AOI (Figure 6a,c). This effect can be attributed to the increasing coupling of the incidence light to the longitudinal plasmon resonance of the tubes, which results in an increased resonant absorption and broadening of the band, due to overlapping of the transversal and longitudinal mode. This observation is in line with the expected ENZ resonance at slightly higher wavelength than the dominating ENP resonance from the theoretical considerations (Figure 3) and is also observed in the full wave simulations even though overlaid by interference fringes (Figure 6a). In contrast to that, for s-polarized light an increase in reflectance is observed with increasing AOI and no broadening of the band in the relevant range over 1400 nm (Figure 6b,d) is observed, since s-polarized light only couples to the transversal mode. At a wavelength of around 2400 nm the behavior with increasing AOI changes and with increasing AOI the reflectance decreases (Figure 6d). This discontinuity can be assigned to a change in sign of the permittivity at that wavelength and is known for hyperbolic metamaterials.[3]

Additionally, for all samples for wavelength below 1500 nm it is evident that the maxima of the thin film interference fringes shift to lower wavelength with increasing AOI, as it is expected for a dielectric behavior. This behavior changes in the expected range of hyperbolicity (>1500 nm) where nearly no shift of the interference fringes is observed, indicating that the permittivity is near the ENZ or ENP condition for p- and s-polarization, respectively.[50] So, all of the data indicate a hyperbolic behavior of both samples in the NIR range.

There are slight differences in the position of the resonances and geometrical parameters for the simulation and experimental data, which probably can be assigned to inhomogeneities of the

prepared ITO nanotube arrays (Figure 2). But, since the trends of the simulation and experimental data are the same, a hyperbolic behavior of the new metamaterial is supported by the simulations. Additionally, the simulations indicate further design parameters such as impact of underlaying materials and geometrical parameters to precisely tailor the optical response of the wire metamaterial (See Supporting Information, S13 – S16) and the strong dependency on the plasma frequency of the ITO paves the way to electrically tunable hyperbolic materials.[33,35]

Conclusions

In summary we introduce a new liquid-phase deposition technique for the fabrication of a high aspect ratio ITO nanotube metamaterial by a template-based approach. The optical properties of the deposited ITO in the hybrid material are tailored by a post annealing step influencing the oxygen vacancy doping. The anisotropic permittivity of the tube metamaterial is theoretically determined and the effect of the post-annealing and geometrical parameters is investigated experimentally and supported by optical simulations. A hyperbolic behavior in the near infrared range is introduced by designed material parameters, which is derived from reflectance and extinction measurements and confirmed by the simulation data. Additionally, an anisotropic plasmonic absorption is found in the metamaterial with different bandwidth for s- and p-polarized light. Since the optical response is shown to be strongly dependent on the plasma frequency of ITO, which is electrically tailorable, the new metamaterial opens new perspectives in the direction of electro-optically switchable hyperbolic metamaterials.

Methods

Substrate/template fabrication. A polished silicon wafer (100 orientation) was magnetron sputter coated with a Ti adhesion layer (8 nm, 150W, RF), a tungsten interlayer (50 nm, 150W, RF) and an aluminum layer (1000 nm, 250W, DC). The silicon wafer is afterwards cut into squares

with 1.4 cm x 1.4 cm edge length. The aluminum layer was anodized in a self-made sample holder in a 0.3 M oxalic acid electrolyte at 5°C, applying an anodic potential of 40 V. For the plane thin film substrates, the anodization was stopped after 30 s, after the current stabilizes, to only oxidize the top layer of the aluminum, resulting in a plane layer of aluminum oxide of about 30 nm on top of the thick aluminum layer (Inset, Figure 1a). The anodic aluminum oxide (AAO) templates were prepared by a two-step anodization process under the same conditions as for the plane substrates. The first anodization step was conducted for 5 min and the oxide layer was afterwards removed in a mixture of phosphoric acid (6 wt%) and chromic acid (1.8 wt%) at 60°C for 45 min. The second anodization was conducted with the same parameters as the first until the current started to strongly decrease as the pores grew to the tungsten layer and tungsten starts to be oxidized. After the anodization the sample is rinsed with water and ethanol and dipped in diluted H_3PO_4 (5 wt%) for 45 min to widen the pores.

ITO thin film and nanotube deposition. The deposition of ITO onto the plane substrate or into the pores of the AAO template is conducted by the same protocol. Prior to the deposition the substrate/template is dipped in H_2O_2 solution (30%) to render the surface hydrophilic and rinsed with water and acetone. As ITO precursor a 0.1 M solution of $In(NO_3)_3$ in EtOH is prepared and 0.01 M $SnCl_4$ is added and stirred until a homogeneous transparent solution is obtained. The solution is prepared directly before the ITO deposition. The substrate/template is placed in the precursor solution, vacuum is applied to the vessel (~10^{-2} mbar) and kept for about 3 min to achieve complete infiltration. The samples are taken from the solution, immediately put on a spin coating system and excess precursor is removed at 2000 rpm for 30 s. After the spin coating the samples are dried in an oven with air atmosphere at 300°C for 15 min, whereby the precursor is converted to ITO. The deposition cycle is repeated until the desired ITO thickness is reached. After

26

the last deposition cycle the samples are post-annealed in a precisely controlled static atmosphere in a quartz tube in a tube furnace. For the high vacuum annealing the quartz tube is connected to a turbo vacuum pump and for the H_2/Ar annealing a static Varigon H5 (5% H_2/95% Ar) is generated in the quartz tube. The annealing is carried out at 450°C for 3 h.

Characterization Methods. An ATC Orion 5 UHV sputter system was employed for sputter coating. SEM images and EDX measurements were acquired using a Hitachi Regulus SU8230 equipped with a Oxford Ultim Max 100 EDX detector. UV-Vis-NIR measurements were carried out with a Cary 5000 spectrometer (Agilent Technologies Inc.) equipped with a praying mantis setup for measurement in diffusive reflectance. TEM images were taken with a Hitachi HT7800. XPS spectra were obtained with a PHI 5000 VersaProbe III x-ray photoelectron spectrometer after Ar sputtering the surface of the sample for 10 min with an acceleration voltage of 3 kV. XRD measurements were conducted with a Bruker D8 Advance. Polarization dependent reflection measurements were obtained with a PerkinElmer Lambda1050 spectrometer equipped with an URA accessory. Ellipsometry measurements were carried out at a Sentech SE850 ellipsometer.

Numerical Simulations. Numerical simulations were performed using COMSOL Multiphysics, wave optics module. A hexagonal unit cell of the metamaterial was considered with periodic boundary conditions. Absorbing boundary conditions were applied in the propagation direction. Due to the subwavelength operating regime, no diffraction orders are present and the total reflectance is reported in all numerical studies.

ASSOCIATED CONTENT

Supporting Information.

The following files are available free of charge.

additional data (file type, i.e., PDF)

AUTHOR INFORMATION

Corresponding Author

*E-mail: sebastian.polarz@aca.uni-hannover.de

E-mail: atefeh.habibpoor@hot.uni-hannover.de

E-mail: antonio.calalesina@hot.uni-hannover.de

Author Contributions

T.H. and A.H. contributed equally to this work. T.H. performed the experimental investigations and data evaluation. A.H. provided guides through modelling and numerical simulations. T.H. and A.H. contributed mainly to writing the manuscript, each having their own shares regarding experimental and simulation discussions, respectively. S.P. initiated the project. S.L. helped write the manuscript. The overall supervisions were performed by S.P. and A.C.L. and secured funding. All authors took part in revising the manuscript. All authors have given approval to the final version of the manuscript. ‡These authors contributed equally. (match statement to author names with a symbol)

ACKNOWLEDGMENT

REFERENCES

(1) Yao, J.; Liu, Z.; Liu, Y.; Wang, Y.; Sun, C.; Bartal, G.; Stacy, A. M.; Zhang, X. Optical Negative Refraction in Bulk Metamaterials of Nanowires. *Science* **2008**, *321* (5891), 930–930. https://doi.org/10.1126/science.1157566.

(2) Liu, Z.; Lee, H.; Xiong, Y.; Sun, C.; Zhang, X. Far-Field Optical Hyperlens Magnifying Sub-Diffraction-Limited Objects. *Science* **2007**, *315* (5819), 1686–1686. https://doi.org/10.1126/science.1137368.

(3) Hoffman, A. J.; Alekseyev, L.; Howard, S. S.; Franz, K. J.; Wasserman, D.; Podolskiy, V. A.; Narimanov, E. E.; Sivco, D. L.; Gmachl, C. Negative Refraction in Semiconductor Metamaterials. *Nat. Mater.* **2007**, *6* (12), 946–950. https://doi.org/10.1038/nmat2033.

(4) Orlov, A. A.; Voroshilov, P. M.; Belov, P. A.; Kivshar, Y. S. Engineered Optical Nonlocality in Nanostructured Metamaterials. *Phys. Rev. B* **2011**, *84* (4), 045424. https://doi.org/10.1103/PhysRevB.84.045424.

(5) Kanehara, M.; Koike, H.; Yoshinaga, T.; Teranishi, T. Indium Tin Oxide Nanoparticles with Compositionally Tunable Surface Plasmon Resonance Frequencies in the Near-IR Region. *J. Am. Chem. Soc.* **2009**, *131* (49), 17736–17737. https://doi.org/10.1021/ja9064415.

(6) Atkinson, R.; Hendren, W. R.; Wurtz, G. A.; Dickson, W.; Zayats, A. V.; Evans, P.; Pollard, R. J. Anisotropic Optical Properties of Arrays of Gold Nanorods Embedded in Alumina. *Phys. Rev. B* **2006**, *73* (23), 235402. https://doi.org/10.1103/PhysRevB.73.235402.

(7) Starko-Bowes, R.; Atkinson, J.; Newman, W.; Hu, H.; Kallos, T.; Palikaras, G.; Fedosejevs, R.; Pramanik, S.; Jacob, Z. Optical Characterization of Epsilon-near-Zero, Epsilon-near-Pole, and Hyperbolic Response in Nanowire Metamaterials. *J. Opt. Soc. Am. B* **2015**, *32* (10), 2074–2080. https://doi.org/10.1364/JOSAB.32.002074.

(8) Padilla, W. J.; Averitt, R. D. Imaging with Metamaterials. *Nat. Rev. Phys.* **2022**, *4* (2), 85–100. https://doi.org/10.1038/s42254-021-00394-3.

(9) Anker, J. N.; Hall, W. P.; Lyandres, O.; Shah, N. C.; Zhao, J.; Van Duyne, R. P. Biosensing with Plasmonic Nanosensors. *Nat. Mater.* **2008**, *7* (6), 442–453. https://doi.org/10.1038/nmat2162.

(10) Noginov, M. A.; Li, H.; Barnakov, Y. A.; Dryden, D.; Nataraj, G.; Zhu, G.; Bonner, C. E.; Mayy, M.; Jacob, Z.; Narimanov, E. E. Controlling Spontaneous Emission with Metamaterials. *Opt. Lett.* **2010**, *35* (11), 1863–1865. https://doi.org/10.1364/OL.35.001863.

(11) Hulteen, J. C.; Martin, C. R. A General Template-Based Method for the Preparation Ofnanomaterials. *J. Mater. Chem.* **1997**, *7* (7), 1075–1087. https://doi.org/10.1039/A700027H.

(12) Yao, J.; Wang, Y.; Tsai, K.-T.; Liu, Z.; Yin, X.; Bartal, G.; Stacy, A. M.; Wang, Y.-L.; Zhang, X. Design, Fabrication and Characterization of Indefinite Metamaterials of Nanowires. *Philos. Trans. R. Soc. Math. Phys. Eng. Sci.* **2011**, *369* (1950), 3434–3446. https://doi.org/10.1098/rsta.2011.0159.

(13) Simovski, C. R.; Belov, P. A.; Atrashchenko, A. V.; Kivshar, Y. S. Wire Metamaterials: Physics and Applications. *Adv. Mater.* **2012**, *24* (31), 4229–4248. https://doi.org/10.1002/adma.201200931.

(14) Shekhar, P.; Atkinson, J.; Jacob, Z. Hyperbolic Metamaterials: Fundamentals and Applications. *Nano Converg.* **2014**, *1* (1), 14. https://doi.org/10.1186/s40580-014-0014-6.

(15) Li, S. Q.; Guo, P.; Zhang, L.; Zhou, W.; Odom, T. W.; Seideman, T.; Ketterson, J. B.; Chang, R. P. H. Infrared Plasmonics with Indium–Tin-Oxide Nanorod Arrays. *ACS Nano* **2011**, *5* (11), 9161–9170. https://doi.org/10.1021/nn203406f.

(16) Boltasseva, A.; Atwater, H. A. Low-Loss Plasmonic Metamaterials. *Science* **2011**, *331* (6015), 290–291. https://doi.org/10.1126/science.1198258.

(17) Naik, G. V.; Shalaev, V. M.; Boltasseva, A. Alternative Plasmonic Materials: Beyond Gold and Silver. *Adv. Mater.* **2013**, *25* (24), 3264–3294. https://doi.org/10.1002/adma.201205076.

(18) Naik, G. V.; Kim, J.; Boltasseva, A. Oxides and Nitrides as Alternative Plasmonic Materials in the Optical Range [Invited]. *Opt. Mater. Express* **2011**, *1* (6), 1090–1099. https://doi.org/10.1364/OME.1.001090.

(19) Wang, Y.; Capretti, A.; Negro, L. D. Wide Tuning of the Optical and Structural Properties of Alternative Plasmonic Materials. *Opt. Mater. Express* **2015**, *5* (11), 2415–2430. https://doi.org/10.1364/OME.5.002415.

(20) Kafaie Shirmanesh, G.; Sokhoyan, R.; Pala, R. A.; Atwater, H. A. Dual-Gated Active Metasurface at 1550 Nm with Wide (>300°) Phase Tunability. *Nano Lett.* **2018**, *18* (5), 2957–2963. https://doi.org/10.1021/acs.nanolett.8b00351.

(21) Askari, H.; Fallah, H.; Askari, M.; Mohmmadieyh, M. C. Electrical and Optical Properties of ITO Thin Films Prepared by DC Magnetron Sputtering for Low-Emitting Coatings. **2014**.

(22) Blair, S. F. J.; Male, J. S.; Cavill, S. A.; Reardon, C. P.; Krauss, T. F. Photonic Characterisation of Indium Tin Oxide as a Function of Deposition Conditions. *Nanomaterials* **2023**, *13* (13), 1990. https://doi.org/10.3390/nano13131990.

(23) Xian, S.; Nie, L.; Qin, J.; Kang, T.; Li, C.; Xie, J.; Deng, L.; Bi, L. Effect of Oxygen Stoichiometry on the Structure, Optical and Epsilon-near-Zero Properties of Indium Tin Oxide Films. *Opt. Express* **2019**, *27* (20), 28618–28628. https://doi.org/10.1364/OE.27.028618.

(24) Lau, K. Y.; Yang, Y.; Zhao, D.; Liu, X.; Qiu, J. Tunable Optical Nonlinearity of Indium Tin Oxide for Optical Switching in Epsilon-near-Zero Region. *Nanophotonics* **2022**, *11* (18), 4209–4219. https://doi.org/10.1515/nanoph-2022-0306.

(25) Del Villar, I.; Zamarreño, C. R.; Hernaez, M.; Sanchez, P.; Arregui, F. J.; Matias, I. R. Generation of Surface Plasmon Resonance and Lossy Mode Resonance by Thermal Treatment of ITO Thin-Films. *Opt. Laser Technol.* **2015**, *69*, 1–7. https://doi.org/10.1016/j.optlastec.2014.12.012.

(26) Ni, J. H.; Sarney, W. L.; Leff, A. C.; Cahill, J. P.; Zhou, W. Property Variation in Wavelength-Thick Epsilon-Near-Zero ITO Metafilm for Near IR Photonic Devices. *Sci. Rep.* **2020**, *10* (1), 713. https://doi.org/10.1038/s41598-020-57556-z.

(27) Salary, M. M.; Mosallaei, H. Electrically Tunable Metamaterials Based on Multimaterial Nanowires Incorporating Transparent Conductive Oxides. *Sci. Rep.* **2017**, *7* (1), 10055. https://doi.org/10.1038/s41598-017-09523-4.

(28) Park, J.; Kang, J.-H.; Kim, S. J.; Liu, X.; Brongersma, M. L. Dynamic Reflection Phase and Polarization Control in Metasurfaces. *Nano Lett.* **2017**, *17* (1), 407–413. https://doi.org/10.1021/acs.nanolett.6b04378.

(29) Jr, H. A. A.; Thureja, P. Active Metasurfaces and Heterostructures for Phase Modulation and Polarization Conversion. In *Active Photonic Platforms 2022*; SPIE, 2022; Vol. PC12196, p PC1219608. https://doi.org/10.1117/12.2633744.

(30) Huang, Y.-W.; Lee, H. W. H.; Sokhoyan, R.; Pala, R. A.; Thyagarajan, K.; Han, S.; Tsai, D. P.; Atwater, H. A. Gate-Tunable Conducting Oxide Metasurfaces. *Nano Lett.* **2016**, *16* (9), 5319–5325. https://doi.org/10.1021/acs.nanolett.6b00555.

(31) Calà Lesina, A.; Goodwill, D.; Bernier, E.; Ramunno, L.; Berini, P. Tunable Plasmonic Metasurfaces for Optical Phased Arrays. *IEEE J. Sel. Top. Quantum Electron.* **2021**, *27* (1), 1–16. https://doi.org/10.1109/JSTQE.2020.2991386.

(32) Yao, Y.; Shankar, R.; Kats, M. A.; Song, Y.; Kong, J.; Loncar, M.; Capasso, F. Electrically Tunable Metasurface Perfect Absorbers for Ultrathin Mid-Infrared Optical Modulators. *Nano Lett.* **2014**, *14* (11), 6526–6532. https://doi.org/10.1021/nl503104n.

(33) Lee, H. W.; Papadakis, G.; Burgos, S. P.; Chander, K.; Kriesch, A.; Pala, R.; Peschel, U.; Atwater, H. A. Nanoscale Conducting Oxide PlasMOStor. *Nano Lett.* **2014**, *14* (11), 6463–6468. https://doi.org/10.1021/nl502998z.

(34) Salary, M. M.; Mosallaei, H. Time-Modulated Conducting Oxide Metasurfaces for Adaptive Multiple Access Optical Communication. *IEEE Trans. Antennas Propag.* **2020**, *68* (3), 1628–1642. https://doi.org/10.1109/TAP.2019.2938613.

(35) Feigenbaum, E.; Diest, K.; Atwater, H. A. Unity-Order Index Change in Transparent Conducting Oxides at Visible Frequencies. *Nano Lett.* **2010**, *10* (6), 2111–2116. https://doi.org/10.1021/nl1006307.

(36) Tice, D. B.; Li, S.-Q.; Tagliazucchi, M.; Buchholz, D. B.; Weiss, E. A.; Chang, R. P. H. Ultrafast Modulation of the Plasma Frequency of Vertically Aligned Indium Tin Oxide Rods. *Nano Lett.* **2014**, *14* (3), 1120–1126. https://doi.org/10.1021/nl4028044.

(37) Guo, P.; Schaller, R. D.; Ketterson, J. B.; Chang, R. P. H. Ultrafast Switching of Tunable Infrared Plasmons in Indium Tin Oxide Nanorod Arrays with Large Absolute Amplitude. *Nat. Photonics* **2016**, *10* (4), 267–273. https://doi.org/10.1038/nphoton.2016.14.

(38) Baxter, J.; Pérez-Casanova, A.; Cortes-Herrera, L.; Calà Lesina, A.; De Leon, I.; Ramunno, L. Dynamic Nanophotonics in Epsilon-Near-Zero Conductive Oxide Films and

Metasurfaces: A Quantitative, Nonlinear, Computational Model. *Adv. Photonics Res.* **2023**, *4* (3), 2200280. https://doi.org/10.1002/adpr.202200280.

(39) Huang, C.; Peng, S.; Liu, X.; Wu, J.; Fu, H.; Lu, L.; Zhang, S.; Li, Q. Manufacturing-Enabled Tunability of Linear and Nonlinear Epsilon-Near-Zero Properties in Indium Tin Oxide Nanofilms. *ACS Appl. Mater. Interfaces* **2023**, *15* (29), 35186–35195. https://doi.org/10.1021/acsami.3c06270.

(40) Wang, H.; Dai, X.; Du, K.; Gao, K.; Zhang, W.; Chua, S. J.; Mei, T. Tuning Epsilon-near-Zero Wavelength of Indium Tin Oxide Film via Annealing. *J. Phys. Appl. Phys.* **2020**, *53* (22), 225108. https://doi.org/10.1088/1361-6463/ab78d8.

(41) Masuda, H.; Fukuda, K. Ordered Metal Nanohole Arrays Made by a Two-Step Replication of Honeycomb Structures of Anodic Alumina. *Science* **1995**, *268* (5216), 1466–1468. https://doi.org/10.1126/science.268.5216.1466.

(42) Ma, K.; Zhou, N.; Yuan, M.; Li, D.; Yang, D. Tunable Surface Plasmon Resonance Frequencies of Monodisperse Indium Tin Oxide Nanoparticles by Controlling Composition, Size, and Morphology. *Nanoscale Res. Lett.* **2014**, *9* (1), 547. https://doi.org/10.1186/1556-276X-9-547.

(43) Kinsey, N.; DeVault, C.; Boltasseva, A.; Shalaev, V. M. Near-Zero-Index Materials for Photonics. *Nat. Rev. Mater.* **2019**, *4* (12), 742–760. https://doi.org/10.1038/s41578-019-0133-0.

(44) Liberal, I.; Engheta, N. Near-Zero Refractive Index Photonics. *Nat. Photonics* **2017**, *11* (3), 149–158. https://doi.org/10.1038/nphoton.2017.13.

(45) Reshef, O.; De Leon, I.; Alam, M. Z.; Boyd, R. W. Nonlinear Optical Effects in Epsilon-near-Zero Media. *Nat. Rev. Mater.* **2019**, *4* (8), 535–551. https://doi.org/10.1038/s41578-019-0120-5.

(46) Peña-Rodríguez, O.; Pal, U. Geometrical Tunability of Linear Optical Response of Silica−Gold Double Concentric Nanoshells. *J. Phys. Chem. C* **2010**, *114* (10), 4414–4417. https://doi.org/10.1021/jp1001034.

(47) Foong, T. R. B.; Shen, Y.; Hu, X.; Sellinger, A. Template-Directed Liquid ALD Growth of TiO2 Nanotube Arrays: Properties and Potential in Photovoltaic Devices. *Adv. Funct. Mater.* **2010**, *20* (9), 1390–1396. https://doi.org/10.1002/adfm.200902063.

(48) Greene, L. E.; Law, M.; Yuhas, B. D.; Yang, P. ZnO−TiO2 Core−Shell Nanorod/P3HT Solar Cells. *J. Phys. Chem. C* **2007**, *111* (50), 18451–18456. https://doi.org/10.1021/jp077593l.

(49) Liu, Y.; Bartal, G.; Zhang, X. All-Angle Negative Refraction and Imaging in a Bulk Medium Made of Metallic Nanowires in the Visible Region. *Opt. Express* **2008**, *16* (20), 15439–15448. https://doi.org/10.1364/OE.16.015439.

(50) Kanungo, J.; Schilling, J. Experimental Determination of the Principal Dielectric Functions in Silver Nanowire Metamaterials. *Appl. Phys. Lett.* **2010**, *97* (2), 021903. https://doi.org/10.1063/1.3462311.